

A Catalog of Quasar Properties from Sloan Digital Sky Survey Data Release 16

QIAOYA WU^{1,2} AND YUE SHEN^{1,3}

¹*Department of Astronomy, University of Illinois at Urbana-Champaign, Urbana, IL 61801, USA*

²*Center for AstroPhysical Surveys, National Center for Supercomputing Applications, University of Illinois at Urbana-Champaign, Urbana, IL 61801, USA*

³*National Center for Supercomputing Applications, University of Illinois at Urbana-Champaign, Urbana, IL 61801, USA*

ABSTRACT

We present a catalog of continuum and emission line properties for 750,414 broad-line quasars included in the Sloan Digital Sky Survey Data Release 16 quasar catalog (DR16Q), measured from optical spectroscopy. These quasars cover broad ranges in redshift ($0.1 \lesssim z \lesssim 6$) and luminosity ($44 \lesssim \log(L_{\text{bol}}/\text{erg s}^{-1}) \lesssim 48$), and probe lower luminosities than an earlier compilation of SDSS DR7 quasars. Derived physical quantities such as single-epoch virial black hole masses and bolometric luminosities are also included in this catalog. We present improved systemic redshifts and realistic redshift uncertainties for DR16Q quasars using the measured line peaks and correcting for velocity shifts of various lines with respect to the systemic velocity. About 1%, 1.4%, and 11% of the original DR16Q redshifts deviate from the systemic redshifts by $|\Delta V| > 1500 \text{ km s}^{-1}$, $|\Delta V| \in [1000, 1500] \text{ km s}^{-1}$, and $|\Delta V| \in [500, 1000] \text{ km s}^{-1}$, respectively; about 1900 DR16Q redshifts were catastrophically wrong ($|\Delta V| > 10,000 \text{ km s}^{-1}$). We demonstrate the utility of this data product in quantifying the spectral diversity and correlations among physical properties of quasars with large statistical samples.

Keywords: black hole physics — galaxies: active — quasars: general — surveys

1. INTRODUCTION

Wide-field spectroscopic surveys such as the Sloan Digital Sky Survey have greatly increased the inventory of quasars over broad ranges in redshift and luminosity (e.g., Schneider et al. 2010; Shen et al. 2011; Dawson et al. 2013; Pâris et al. 2017; Lyke et al. 2020). Optical spectra from these surveys provide rich information on the physical properties of these quasars, enabling detailed statistical studies of their abundance, accretion parameters, and correlations among physical properties.

Using optical spectroscopy from the SDSS I-II legacy survey, Shen et al. (2011) measured spectral properties for 105,783 quasars included in SDSS DR7. Such spectral measurements have been extended to later SDSS quasar catalogs (e.g., Rakshit et al. 2020) for larger samples of quasars observed in SDSS-III (Eisenstein et al. 2011) and SDSS-IV (Blanton et al. 2017). These later generations of SDSS surveys target quasars to fainter

magnitudes than the SDSS-I/II survey, with upgraded SDSS optical spectrographs (Smee et al. 2013), thus expanding the dynamical range in SDSS quasar samples.

In this work, we measure spectral properties for the $\sim 750\text{k}$ quasars included in the latest SDSS DR16 quasar catalog (Lyke et al. 2020). As a major update to the SDSS DR7 quasar catalog presented in Shen et al. (2011), we present measurements for a more comprehensive list of emission lines and refined systemic redshifts based on these spectral measurements. We also compile derived quantities including black hole mass and Eddington ratio estimates to facilitate statistical studies of SDSS quasars. This paper is organized as follows. In §2 we describe the input data of the catalog. We detail our spectral measurements in §3 and describe the compiled properties in §4. We present example applications of this catalog in §5 and conclude in §6. Throughout this paper, we adopt a flat Λ CDM cosmology with $\Omega_{\Lambda} = 0.7$, $\Omega_M = 0.3$ and $H_0 = 70 \text{ km s}^{-1} \text{ Mpc}^{-1}$.

2. DATA

We start from the DR16Q catalog, which includes 750,414 quasars observed through SDSS-I/II/III/IV.

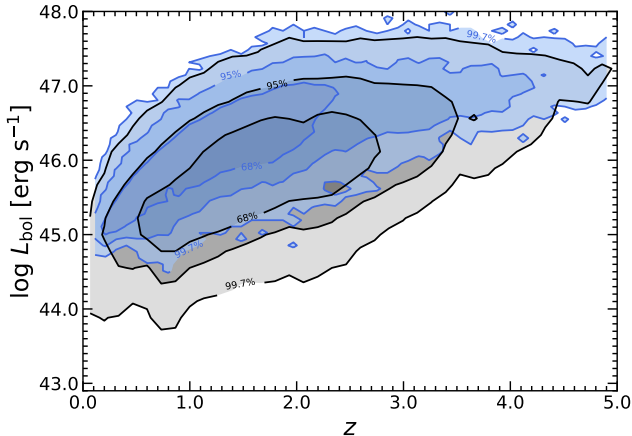


Figure 1. Distribution of quasars in the redshift and luminosity space. The DR16Q sample is shown as black contours. The blue contours are for the SDSS DR7 quasars compiled in Shen et al. (2011). Enclosed percentiles are marked for each contour level.

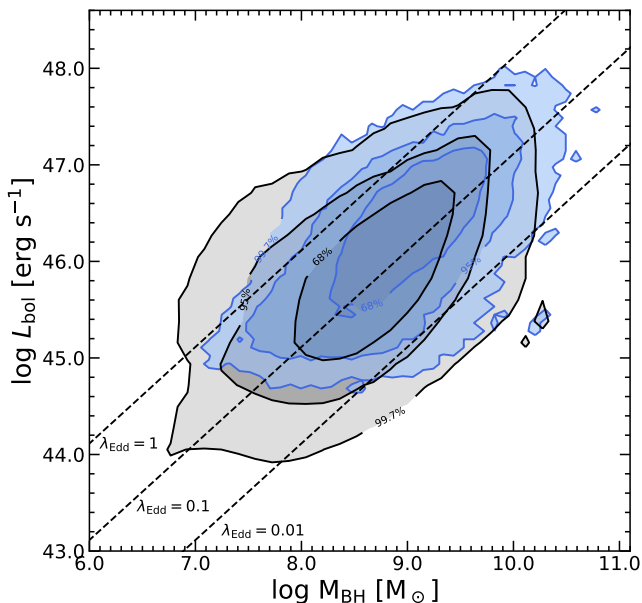


Figure 2. Distribution of quasars in the BH mass and bolometric luminosity space. The DR16Q sample is shown as black contours. The blue contours are for the SDSS-DR7 quasars compiled in Shen et al. (2011). Enclosed percentiles are marked for each contour level. We caution that quasars with apparent Eddington ratios $\lambda_{\text{Edd}} > 1$ are likely caused by uncertainties in the BH mass estimates.

This quasar catalog represents the final quasar sample from SDSS-IV (i.e., SDSS-IV DR17 does not contain new quasars). More than half of these quasars are nearly discovered in SDSS-IV. For completeness, DR16Q also includes quasars observed in previous generations

of SDSS, specifically quasars from legacy SDSS-I/II (DR7Q, Schneider et al. 2010) and SDSS-III (DR12Q, Pâris et al. 2017). If a quasar is re-observed in SDSS-IV, then the SDSS-IV observation is taken as the primary spectroscopy for that object. Cross-matching sources in DR16Q with the DR7 quasar catalog (Schneider et al. 2010), there are 85 bona fide quasars included in DR7Q that are missing from DR16Q. We do not attempt to recover these 85 quasars since their measurements are included in Shen et al. (2011). For initial redshift used for our spectral fitting, we adopt the best redshift in DR16Q (Column ‘Z’ in Lyke et al. 2020) and denote it as z_{DR16Q} .

SDSS optical spectroscopy has been obtained with the SDSS-I/II spectrographs for DR7 data and the upgraded BOSS spectrographs (Smee et al. 2013) for SDSS-III and SDSS-IV data. The characteristics of these spectroscopic data are similar but differ in details: DR7 spectra have a wavelength coverage of $\sim 3800 - 9200 \text{ \AA}$ while BOSS spectra have a wavelength coverage of $\sim 3650 - 10400 \text{ \AA}$. The spectral resolution is roughly the same, $R \sim 2000$ and both SDSS-I/II and SDSS-III/IV spectra are stored in vacuum wavelength with a pixel dispersion of 69 km s^{-1} (i.e., the wavelength array is logarithmically binned with a dispersion of $d \log_{10} \lambda = 10^{-4}$). The BOSS spectrographs accommodate a total of 1000 fibers ($2''$ in diameter) while the legacy SDSS spectrographs accommodated 640 fibers ($3''$ in diameter). In addition, BOSS spectrographs have improved throughput than the legacy SDSS spectrographs, resulting in higher S/N at fixed magnitude and exposure time than legacy SDSS I-II spectra.

In Fig. 1 and Fig. 2 we show the distributions of DR16Q quasars in the redshift-luminosity plane and the black hole mass-luminosity plane, using spectral measurements described in §3. Compared with quasars in the DR7Q catalog, DR16Q quasars probe fainter luminosities, given improved sensitivity of the BOSS spectrographs that allowed targeting to fainter flux limits.

3. SPECTRAL MEASUREMENTS

We follow the practice in earlier work (e.g., Shen et al. 2016, 2019) to fit the SDSS spectra with a global continuum+emission lines model, using the public code PyQSOFIT (e.g., Guo et al. 2018; Shen et al. 2019) developed by our group. Minor custom adjustments of the fitting constraints are made to produce more robust spectral measurements of DR16Q quasars. The input fitting parameter file is provided in the supplemental materials¹.

¹ https://github.com/QiaoyaWu/sdss4.dr16q_tutorial

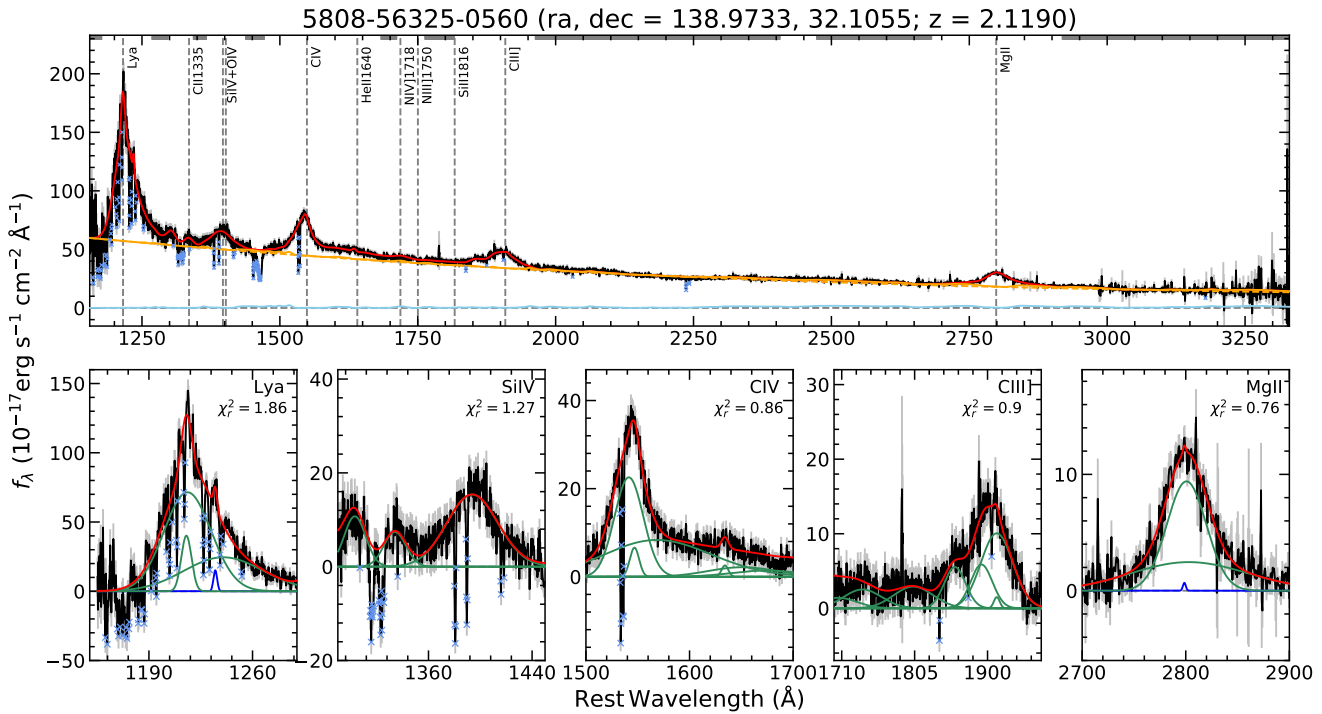


Figure 3. An example of quality assessment (QA) plot for our global spectral fitting approach. The top panel shows the continuum (orange) and Fe II (sky-blue) model components; the red line is the global model combining all continuum and emission line components. The light blue crosses are pixels within the continuum and emission-line-fitting windows that are masked as absorption and excluded from the model fit. The gray line segments near the top of the panel indicate the windows used for the continuum + Fe II fit. The bottom panels present the emission-line fits for several line complexes, where the green (blue) lines represent broad (narrow) Gaussian components within that line complexes.

The detailed methodology of our spectral fitting is described in earlier work (Shen et al. 2016, 2019; Guo et al. 2018). In brief, we first correct the observed spectrum for Milky Way reddening using the dust map from Schlegel et al. (1998) (updated to the values in Schlafly & Finkbeiner (2011)) and the Cardelli et al. (1989) extinction curve with $R_V = 3.1$. The observed spectrum is then shifted to the quasar rest-frame using the default redshift in DR16Q to be fitted by the model.

The continuum model fits the dereddened, deredshifted spectrum in several relatively line-free regions with the combination of a power law and a third-order polynomial. These continuum-fitting windows are listed in Table 1. The additive (positive-definite) polynomial component is introduced to fit objects with peculiar continuum shapes, e.g., due to peculiar intrinsic dust reddening (e.g., Shen et al. 2019). In addition to the power-law and polynomial components, we include the optical and UV Fe II emission using empirical templates in the same continuum-fitting windows (Boroson & Green 1992; Vestergaard & Wilkes 2001; Tsuzuki et al. 2006; Salviander et al. 2007). The continuum and the Fe II emission form a pseudo-continuum, which we subtract from the original spectrum to form a line-only

spectrum. We then fit the line-only spectrum with a set of Gaussians in logarithmic wavelength space over several line complexes. The details of the line complexes in the fit are summarized in Table 2.

As discussed in Shen et al. (2019), we do not include additional model components, such as the Balmer continuum and host galaxy emission, in our spectral fits. This is because the limited S/N and spectral coverage of our spectra often do not allow more sophisticated model fits and will return unreliable results for the majority of quasars with low-to-moderate spectral S/N. Nevertheless, the PyQSOFIT code can turn on these optional model components in the fit.

For several narrow emission (stellar absorption) lines of interest, our global model often does not provide an accurate estimate of the local continuum level around them, resulting in biased line measurements. To remedy this, we re-fit these emission/absorption features with a local continuum+line model. The details of the local fits around these lines are summarized in Table 3.

Table 1. Rest-frame Continuum Fitting Windows

Continuum windows (1)	Fitting range [\AA] (2)
1	1150-1170
2	1275-1290
3	1350-1360
4	1445-1465
5	1690-1705
6	1770-1810
7	1970-2400
8	2480-2675
9	2925-3400
10	3775-3832
11	4000-4050
12	4200-4230
13	4435-4640
14	5100-5535
15	6005-6035
16	6110-6250
17	6800-7000
18	7160-7180
19	7500-7800
20	8050-8150

Finally, high-redshift quasar spectra are often affected by intervening or intrinsic absorption lines. Following earlier work (e.g., Shen et al. 2019), we remedy the effect of absorption lines with an iterative approach to reject pixels fall 3σ below the original model fit and re-fit. This automated absorption-line mitigation scheme does a good job reducing the impact from narrow absorption features in the fit, but improvement in objects affected by broad absorption troughs is only mild.

We measure the continuum and emission-line properties using the best-fit model parameters. To estimate the uncertainties of these spectral measurements, we use a Monte Carlo approach (e.g., Shen et al. 2011, 2019): the original spectrum is perturbed by adding a Gaussian random deviate at each pixel using the reported spectral flux errors to generate a mock spectrum; we fit the mock spectra from 25 random trials and take the semi-amplitude of the 16th and 84th percentile range as the measurement uncertainty in the reported spectral property. We have tested with more random trials (e.g., 100) for a random subset of quasars and did not find significant differences in the uncertainty estimates. We therefore adopt 25 Monte Carlo trials per quasar to speed up the spectral fits.

Table 2. Line Fitting Parameters

Complex (1)	Fitting range [\AA] (2)	$N_{\text{pix,max}}$ (3)	Line (4)	n_{gauss} (5)
H α	6400-6800	264	broad H α	3
			narrow H α	1
			[NII]6549	1
			[NII]6585	1
			[SII]6718	1
			[SII]6732	1
H β	4640-5100	411	broad H β	3
			narrow H β	1
			[OIII]4959 core	1
			[OIII]5007 core	1
			[OIII]4959 wing	1
			[OIII]5007 wing	1
			broad HeII 4687	1
			narrow HeII 4687	1
Mg II	2700-2900	311	broad Mg II	2
			narrow Mg II	1
C III]	1700-1970	641	C III]	2
			Si III] 1892	1
			Al III 1857	1
			[Si II] 1816	1
			N III 1750	1
			N IV 1718	1
C IV	1500-1700	544	C IV	3
			broad HeII 1640	1
			narrow HeII 1640	1
			broad OIII 1663	1
			narrow OIII 1663	1
Si IV	1290-1450	508	broad SiIV/OIV]	2
			C II 1335	1
			O I 1304	1
Ly α	1150-1290	499	Ly α	3
			Nv 1240	1

Table 3. Local Line Fitting Parameters

Complex (1)	Fitting range [\AA] (2)	$N_{\text{pix,max}}$ (3)	Line (4)	n_{gauss} (5)
Ca II	3900-3960	67	Ca II 3934	2
[O II]	3650-3800	175	[O II] 3728	1
[Ne V]	3380-3480	127	[Ne V] 3426 core	1
			[Ne V] 3426 wing	1

4. CATALOG COMPILATION

We compile our spectral measurements and derived quantities in Table 4. The basic spectral measurements include properties of the continuum (and Fe II emission) and prominent broad and narrow emission lines in quasar spectra. Our spectral fits are fully automated with various fitting restrictions to reduce the rate of catastrophic failures of the fitting. Quantities not measured (e.g., not covered by the spectrum) have associated errors = -1 . Because of the large size of the sample and diverse spectral properties of quasars, there are

still cases where the fitting results might be unreliable. We provide all the measured properties, associated uncertainties and quality flags in Table 4. These reported quantities can be used to select a cleaned sample of measurements. In the case of a specific line, we recommend the following quality cuts:

- line flux / flux error > 2 ,
- $38 < \log(L_{\text{line}}/\text{erg s}^{-1}) < 48$,
- $N_{\text{pix,line complex}} > 0.5 \times N_{\text{max}}$.

Line measurements that do not meet the first cut (i.e., the line is detected at $> 2\sigma$) might still be valid, but will be noisy and potentially biased. The last two criteria are particularly useful to remove rare cases where the line is unconstrained due to data gaps in the spectrum, and N_{max} is the maximum number of available pixels in SDSS spectra for a given line complex.

We also pay specific attention to the C IV fits. Since the C IV FWHM is an essential quantity in the estimation of virial BH masses and we do not impose width constraints in the three Gaussians fit to the entire C IV profile, we reject any Gaussians with fluxes less than 5% of the total C IV flux in measuring the C IV FWHM. This treatment efficiently accounts for cases where one or more Gaussians are adversely fit to noise spikes in the spectrum. The other two broad emission lines used for virial BH mass estimation, H β and Mg II, do not require this additional processing as the broad-line profile is usually well fit by the model per our visual inspection.

In addition to these basic spectral measurements, we provide derived quantities, as detailed below.

4.1. Bolometric luminosities, black hole masses and Eddington ratios

We estimate the bolometric luminosity L_{bol} of the quasar using the measured continuum luminosity (Fe II emission excluded) at rest-frame wavelengths of 5100 Å, 3000 Å, and 1350 Å, depending on the redshift of the quasar. Bolometric corrections (BC) are derived from the mean spectral energy distribution of quasars in Richards et al. (2006), with BC = 9.26, 5.15, 3.81 at the three wavelengths, respectively. Whenever possible, we use the 3000 Å continuum luminosity to estimate L_{bol} because it has less host contamination than the 5100 Å luminosity and suffers less from reddening and variability than the 1350 Å luminosity. Measurement uncertainties in L_{bol} are propagated from measurement uncertainties in the monochromatic luminosity used. We caution that quasar SEDs can vary significantly among individual objects, and these bolometric luminosity estimates based on a single monochromatic continuum luminosity

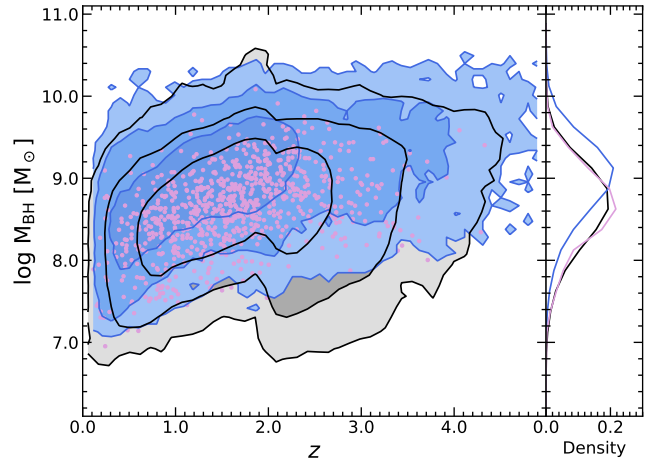


Figure 4. Distribution of quasars in the redshift and BH mass space. The DR16Q sample is shown in black contours; the SDSS-DR7 quasars are shown in blue contours; the SDSS-RM sample (Shen et al. 2019) is plotted in pink points. The apparent discontinuity around $z \sim 2$ is caused by the switch from Mg II BH masses to C IV masses, as discussed in §5.1.

could have substantially larger systematic uncertainties for individual objects (e.g., Richards et al. 2006). All luminosities are calculated using the ZFIT redshift instead of the improved systemic redshifts described in §4.2 – the luminosity differences from this detail are negligible.

Following previous work (e.g., Shen et al. 2011, 2019), we estimate black hole masses from the continuum and broad emission line measurements. These BH mass estimates are based on the so-called “single-epoch virial BH mass” estimators (e.g., Vestergaard & Peterson 2006). We adopt the same fiducial BH mass recipes on H β , Mg II and C IV as in Shen et al. (2011, 2019). These three BH mass recipes are shown to produce consistent estimates for DR7Q quasars when two lines are available (Shen et al. 2011, and see Fig. 9). Alternative mass recipes can be applied using the compiled continuum and broad-line measurements. However, we caution that it is only valid to apply a BH mass recipe that follows the same spectral fitting methodology as adopted here in order to avoid biases in the measured continuum and broad-line properties.

There are significant systematic uncertainties in these single-epoch BH mass estimates (see discussions in, e.g., Shen 2013), and we caution on any direct physical interpretations with these virial BH masses. In the catalog, uncertainties in the virial BH masses are measurement uncertainties only, and the systematic uncertainties of these BH masses can be as large as ~ 0.4 dex (e.g., Shen 2013).

In the compiled catalog, we provide BH mass estimates based on all three lines ($H\beta$, Mg II, and C IV) whenever available. For the fiducial BH mass, we adopt the $H\beta$ mass for $z < 0.7$; for BOSS data, we use Mg II and C IV mass for $0.7 \leq z < 2.0$ and $z \geq 2.0$, respectively; for SDSS legacy data, we use Mg II and C IV mass for $0.7 \leq z < 1.9$ and $z \geq 1.9$, respectively. Fig. 4 shows the distribution of DR16Q quasars in the BH mass versus redshift plane. These fiducial BH masses and bolometric luminosities are used to calculate the Eddington ratio $\lambda \equiv L_{\text{bol}}/L_{\text{Edd}}$, where $L_{\text{Edd}} = 1.3 \times 10^{38} (M_{\text{BH}}/M_{\odot}) \text{ erg s}^{-1}$ is the Eddington luminosity of the quasar.

4.2. Improved systemic redshifts

Accurate systemic redshift of quasars is crucial to most science applications. As such, extra efforts are often invoked to improve the quasar redshifts produced by the SDSS pipeline (e.g., Hewett & Wild 2010; Shen et al. 2019). The redshift of quasars is mainly constrained by prominent emission line features. However, quasar emission lines are known to have a variety of velocity shifts from the systemic velocity that depend on the line species (e.g., Gaskell 1982; Tytler & Fan 1992; Richards et al. 2002; Shen et al. 2016). Shen et al. (2016) studied velocity shifts between different quasar emission lines and Ca II absorption (from the host galaxy) using a sample of quasars with high S/N from the coadded BOSS spectra in the SDSS-RM project (Shen et al. 2015). Based on these measurements, Shen et al. (2016) provided recipes to correct for the average velocity offset from systemic for different lines, as well as realistic uncertainties of the velocity correction. Using this scheme and our line measurements for DR16Q quasars, we derive improved systemic redshifts for all DR16Q quasars.

The default redshifts in DR16Q are mostly based on the redshifts derived by the SDSS pipeline (Bolton et al. 2012). Lyke et al. (2020) also visually inspected a small fraction of quasars and updated their default redshifts in DR16Q with visual redshifts. The SDSS pipeline redshifts were based on PCA template fitting to the observed spectra, where the quasar templates were constructed from a fixed benchmark sample of quasars. As detailed in Shen et al. (2016), the PCA template fitting does not fully account for the diversity in velocity shifts of various quasar emission lines, and only correct for the average velocity shift appropriate for the luminosity ranges probed by the benchmark sample. This is particularly a problem for high-redshift quasars where the strong broad C IV line dominates the redshift estimation. The C IV line is generally blueshifted from the systemic velocity, with its blueshift increasing with quasar

luminosity (e.g., Gaskell 1982; Richards et al. 2002; Shen et al. 2016). The default SDSS redshift pipeline does not address well this luminosity-dependent velocity shift of C IV (and a few other high-ionization lines showing similar behaviors), and thus would lead to biased redshifts across the luminosity range of quasars.

We follow the recipe in Shen et al. (2016) to correct for the average intrinsic velocity shifts of different lines, with additional luminosity dependence for three high-ionization lines: C IV, He II 1640 and Si IV. However, realizing that the luminosity range probed by DR16Q quasars extends to fainter luminosities than those of the SDSS-RM quasars used in the calibration of velocity shifts in Shen et al. (2016), we force the velocity shifts of C IV, He II 1640 and Si IV to be zero below $\log(L_{1700}/\text{erg s}^{-1}) = 44.5$. This modification is necessary so that we do not artificially introduce redshifted high-ionization lines for the low-luminosity quasars in DR16Q. For secure line redshift measurements, we only use lines detected at $> 2\sigma$ and require the spectrum covers at least 50% of the pixels in the line complex. The individual lines from which we estimate $z_{\text{sys,line}}$ are: $H\beta_{\text{br}}$, [O III] 5007, Ca II 3934, [O II] 3728, [Ne V] 3426, Mg II, C III], He II 1640, C IV, Si IV. By default the peak from the full line profile is used (broad+narrow component) unless specified otherwise. However, we find many quasars have inaccurate fits for He II 1640 and [Ne V] 3426, which would lead to biased redshift estimates. We therefore exclude these two lines in the final systemic redshift estimation below. The $z_{\text{sys,line}}$ values for the remaining 8 lines are listed in Table 4.

After deriving the systemic redshift $z_{\text{sys,line}}$ based on individual lines, we derive a mean $z_{\text{sys,mean}}$ from these lines weighted by their individual uncertainties. These redshift uncertainties are the quadratic sum of measurement uncertainties of the line peak and systematic uncertainties from the scatter in the line velocity offset from systemic (e.g., Shen et al. 2016). When calculating the mean systemic redshift using individual z_{line} , we reject outlier z_{line} values that are > 3 times the Median Absolute Deviation from the mean. Compared with individual $z_{\text{sys,line}}$, $z_{\text{sys,mean}}$ produces the best estimate of the true systemic redshift of the quasar, as at times a particular z_{line} is incorrectly measured due to a bad fit. We demonstrate the performance of $z_{\text{sys,mean}}$ with composite spectra (see below). For simplicity, in what follows we use z_{sys} to refer to $z_{\text{sys,mean}}$.

In visual inspection of quasars with redshift differences exceeding 1500 km s^{-1} between z_{DR16Q} and our z_{sys} , we find that many of these quasars have catastrophically incorrect DR16Q redshift. We manually as-

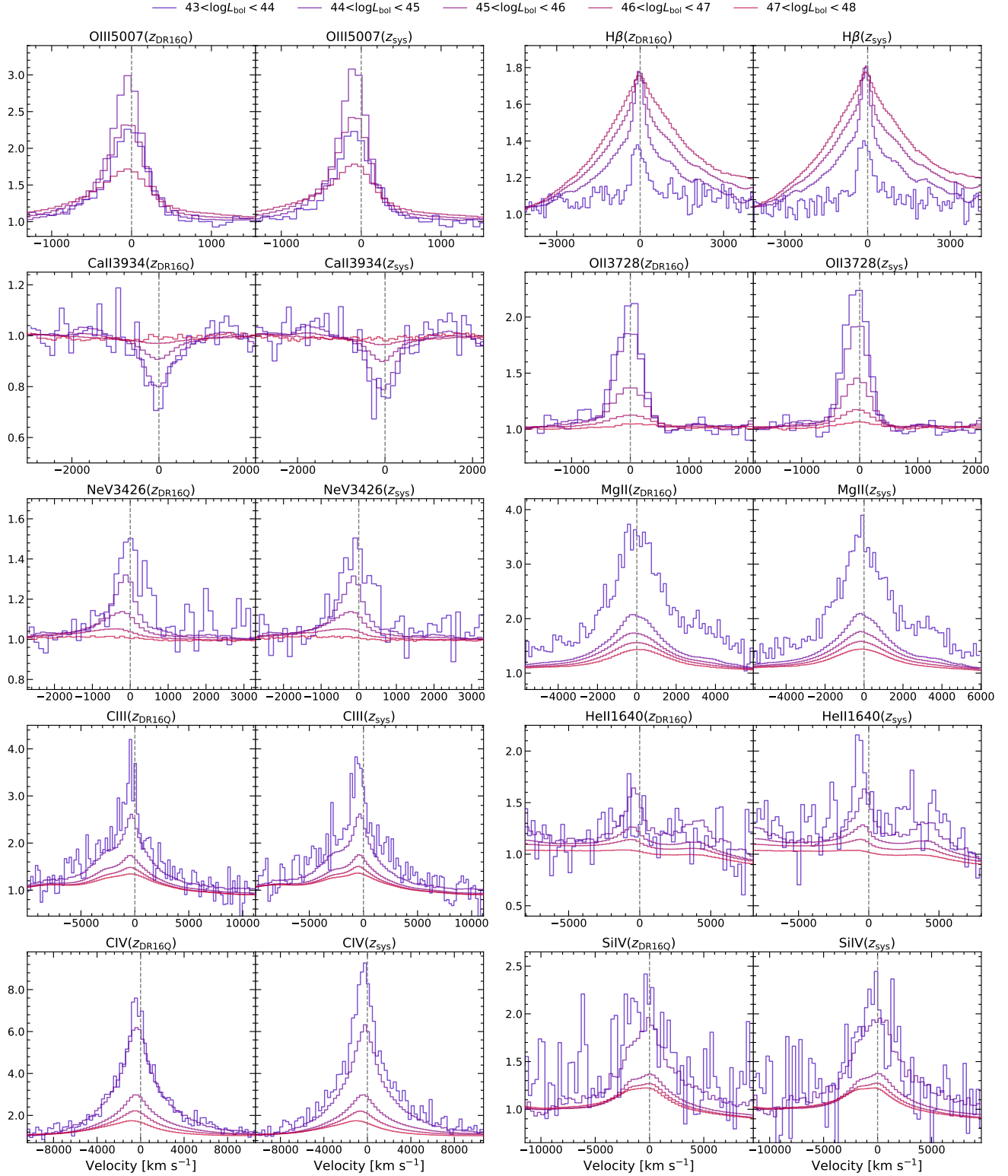


Figure 5. Median composite spectra around several emission/stellar absorption lines of the DR16Q sample, generated using the default DR16Q redshifts (left panels) and the improved systemic redshift (right panels), as a function of quasar luminosity. The improved systemic redshifts make the narrow line features in the composite spectrum sharper, and the peaks of broad lines closer to their expected wavelengths (can be shifted from the systemic velocity).

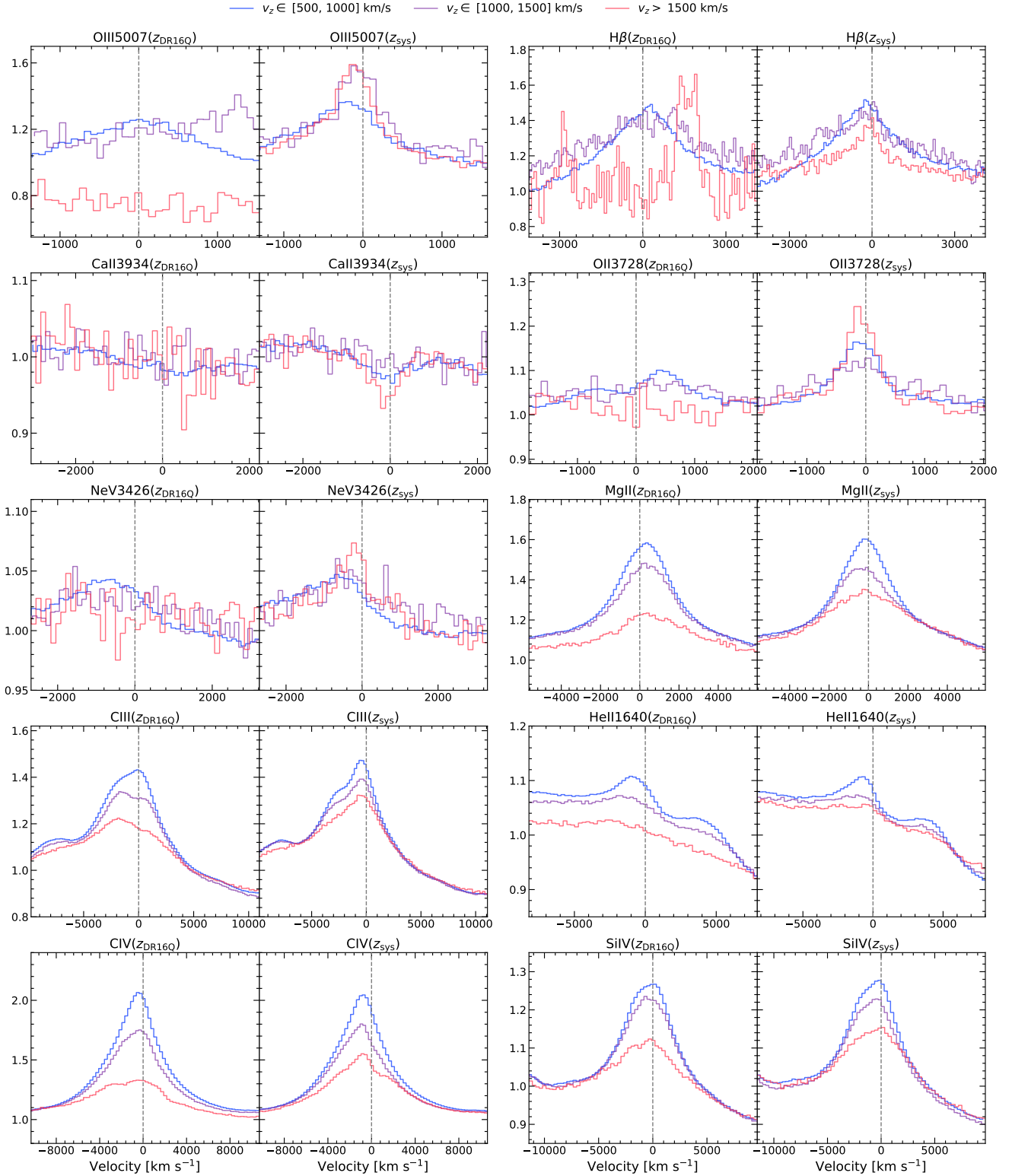


Figure 6. Median composite spectra around several emission/stellar absorption lines of DR16Q quasars with large discrepancies between the default DR16Q redshift and the new systemic redshift, generated using the default DR16Q redshifts (left panels) and the improved systemic redshift (right panels). The new systemic redshifts perform much better than z_{DR16Q} in the statistical sense.

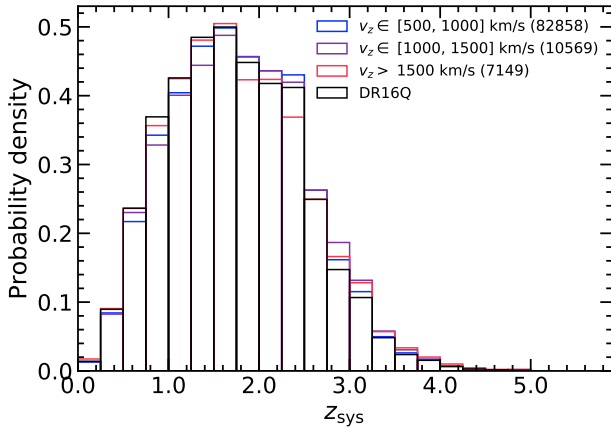


Figure 7. Redshift distributions of DR16Q quasars with large discrepancies between z_{DR16Q} and z_{sys} for the three subsamples shown in Fig. 6. They roughly follow the same redshift distribution of the full DR16Q sample, suggesting no particular redshift failures (of z_{DR16Q}) in certain regime. The numbers of quasars in these subsamples are shown in the top-right legend.

sign redshifts to these quasars, and refit them to derive improved systemic redshifts. The Z_FIT column in the catalog refers to the manual redshift rather than the initial guess z_{DR16Q} for these objects.

Because we use the peak of the line model to measure systemic redshift following earlier work (Shen et al. 2019), we pay specific attention to noisy spikes in the spectrum mistaken as the line peak. This is a problem mainly for C IV and Mg II, where we use the peak from the full model profile (all broad+narrow Gaussians) to measure $z_{\text{sys,line}}$. We therefore reject any Gaussians with fluxes less than 5% of the total line flux before we measure the line peak and $z_{\text{sys,line}}$ from it. There is a different rare situation with C III], where the peak of the C III] complex is dominated by the adjacent Si III] line. Therefore we use the peak of the C III] line (not the entire C III] complex) to measure $z_{\text{line,CIII}}$. Although we have applied these additional criteria in measuring the line-based redshift, we preserve the original line peak measurements in the catalog (Table 4).

We are able to derive systemic redshift estimates for the vast majority of DR16Q quasars. For the remaining small fraction of objects, the spectra are either too noisy to reliably measure line peaks or the spectrum is the superposition of objects at different redshifts (very rare occasions). For those without z_{sys} measurements, we set z_{sys} to be the input redshift of the fit and its error to -1 . The redshifts for these objects are highly uncertain and for some of them even the quasar classification is questionable.

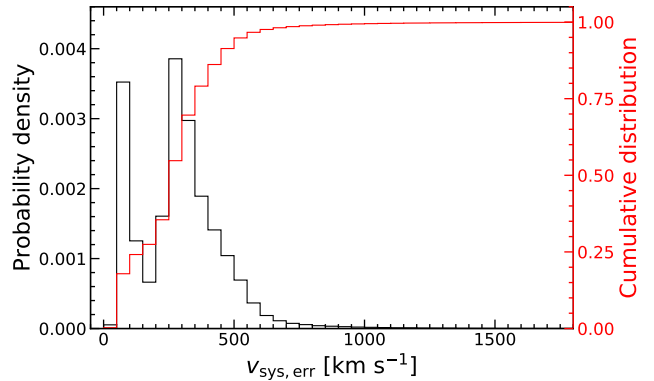


Figure 8. Probability distribution (black) and cumulative distribution (red) of the velocity uncertainty of z_{sys} for the DR16Q sample.

Fig. 5 compares our z_{sys} with z_{DR16Q} using median composite spectra of DR16Q quasars. In this comparison, we divide the sample in different luminosity bins to show any potential luminosity dependence of line shift. For low-ionization broad lines and narrow emission lines, our new redshifts are better than z_{DR16Q} given the slightly sharper profile of the composite line spectrum (in particular for [O II]). The peak locations of [O III] 5007 and Mg II are also more consistent with their expected velocity shifts from the systemic velocity (Shen et al. 2016) using our systemic redshifts.

Furthermore, for high-ionization broad lines such as C IV with a known luminosity dependence of the line velocity shift, our systemic redshifts reproduce this luminosity trend well. On the contrary, the default DR16Q redshifts failed to produce a clear luminosity trend of C IV blueshift. This is expected because the PCA redshifts are dominated by the mean quasar spectrum (the first PCA eigenvector) from the calibration sample, with a fixed average C IV blueshift.

We note that for the majority of DR16Q quasars, the difference between z_{DR16Q} and z_{sys} is less than 500 km s^{-1} ; thus the extra broadening of the lines due to redshift uncertainties in the composite spectra is more obvious in narrow lines than in broad lines. To further demonstrate the improvement of our redshift estimation, we compare the composite spectra for subsets of DR16Q quasars with large differences between z_{DR16Q} and z_{sys} in Fig. 6. This comparison further demonstrates that our systemic redshifts are substantially better than z_{DR16Q} in the statistical sense. We visually inspect these individual quasars with large redshift discrepancies, and conclude that in the vast majority of cases our systemic redshift is indeed better than z_{DR16Q} . On the other hand, there are 141 quasars for which our z_{sys} values are biased by a bad line fit; we fix these 141 quasar

redshifts by assigning a manual redshift based on visual inspection and set the z_{sys} uncertainty to be -2 .

For $\sim 90\%$ of the DR16Q sample, the redshift difference between z_{DR16Q} and our z_{sys} is small ($|\Delta V| \equiv |c\Delta z/(1+z)| < 500 \text{ km s}^{-1}$), indicating that the SDSS redshift pipeline performs well overall. However, 11%, 1.4%, and 1% of the quasars have redshift differences $|\Delta V| \in [500, 1000]$, $|\Delta V| \in [1000, 1500]$ and $|\Delta V| > 1500 \text{ km s}^{-1}$, respectively. We show the redshift distributions of these subsets of quasars in Fig. 7, which show no obvious differences among the three subsets. There are 1943 quasars with $|\Delta V| > 10,000 \text{ km s}^{-1}$, in which case we consider z_{DR16Q} to be catastrophically wrong, as resulting from mis-identified lines in the spectrum by the BOSS pipeline. Our visual inspection of the DR16Q

sample is not exhaustive and likely even incorrect for rare objects, and therefore there are still a small fraction of quasars with incorrect or inaccurate redshifts. But the fraction of such bad redshifts has been greatly reduced with our approach. In particular, a substantial fraction of quasars with $z_{\text{DR16Q}} > 5$ turn out to be lower-redshift quasars.

Finally, in Fig. 8 we show the distribution of uncertainties of our systemic redshifts combining measurement and systematic errors. Low-redshift quasars have smaller redshift uncertainties from narrow emission lines, while quasars with broad lines only in their spectra have redshift uncertainties larger than 200 km s^{-1} . The vast majority of quasars have redshift uncertainties less than 500 km s^{-1} .

Table 4. FITS Catalog Format

Column	Format	Units	Description
SDSS_NAME	STRING		SDSS DR16 designation (J2000)
PLATE	LONG64		Spectroscopic plate number
MJD	LONG64		Spectroscopic MJD
FIBERID	LONG64		Spectroscopic fiber number
RA	DOUBLE	degree	Right ascension (J2000)
DEC	DOUBLE	degree	Declination (J2000)
OBJID	STRING		PLATE-MJD-FIBERID: PyQSOFit output name
IF_BOSS_SDSS	STRING		Source of the input spectrum: BOSS or SDSS
Z_DR16Q	DOUBLE		Best redshift provided by DR16Q
SOURCE_Z_DR16Q	STRING		Source for DR16Q redshift from Lyke et al. (2020)
Z_FIT	DOUBLE		Input redshift for QSOFit; can differ from Z_DR16Q
Z_SYS	DOUBLE		Systemic redshift
Z_SYS_ERR	DOUBLE		Uncertainties of systemic redshift
EBV	DOUBLE		Milky Way extinction $E(B - V)$ from Schlegel et al. (1998) and scaled to match the results in Schlafly & Finkbeiner (2011)
SNR_MEDIAN_ALL	DOUBLE		Median S/N per pixel of the raw spectrum
CONTI_FIT	DOUBLE[5]		Best-fit parameters for the continuum model (PL+poly)
CONTI_FIT_ERR	DOUBLE[5]		Uncertainties in the best-fit continuum parameters
CONTI_FIT_STAT	DOUBLE[2]		Continuum fitting pixel number, reduced χ^2
FEII_UV	DOUBLE[3]		Best-fit parameters for the UV Fe II model
FEII_UV_ERR	DOUBLE[3]		Uncertainties in the best-fit UV Fe II model
FEII_UV_EW	DOUBLE	Å	Rest-frame equivalent width of UV Fe II within 2250-2650 Å
FEII_UV_EW_ERR	DOUBLE	Å	Uncertainties in REW_FE_2250_2650
FEII_OPT	DOUBLE[3]		Best-fit parameters for the optical Fe II model
FEII_OPT_ERR	DOUBLE[3]		Uncertainties in the best-fit optical Fe II model
FEII_OPT_EW	DOUBLE	Å	Rest-frame equivalent width of optical Fe II within 4434-4684 Å
FEII_OPT_EW_ERR	DOUBLE	Å	Uncertainties in REW_FE_4434_4684
LOGL1350	DOUBLE	[erg s ⁻¹]	Continuum luminosity at rest-frame 1350 Å
LOGL1350_ERR	DOUBLE	[erg s ⁻¹]	Uncertainty in LOGL1350

Continued on Next Page...

Table 4 – Continued

Column	Format	Units	Description
LOGL1700	DOUBLE	[erg s ⁻¹]	Continuum luminosity at rest-frame 1700 Å
LOGL1700_ERR	DOUBLE	[erg s ⁻¹]	Uncertainty in LOGL1700
LOGL3000	DOUBLE	[erg s ⁻¹]	Continuum luminosity at rest-frame 3000 Å
LOGL3000_ERR	DOUBLE	[erg s ⁻¹]	Uncertainty in LOGL3000
LOGL5100	DOUBLE	[erg s ⁻¹]	Continuum luminosity at rest-frame 5100 Å
LOGL5100_ERR	DOUBLE	[erg s ⁻¹]	Uncertainty in LOGL5100
		Å, Å, 10 ⁻¹⁷ erg s ⁻¹ cm ⁻² , [erg s ⁻¹], km s ⁻¹ , Å	peak wavelength, 50% flux centroid wavelength, flux, logL _{line} , FWHM, rest-frame equivalent width
HALPHA	DOUBLE[6]	...	For the entire H α profile (narrow and broad lines combined)
HALPHA_BR	DOUBLE[6]	...	For the broad H α component
NII6585	DOUBLE[6]	...	For the narrow [N II] λ 6584 component
HBETA	DOUBLE[6]	...	For the entire H β profile (narrow and broad lines combined)
HBETA_BR	DOUBLE[6]	...	For the broad H β component
HEII4687	DOUBLE[6]	...	For the entire He II λ 4687 profile (narrow and broad lines combined)
HEII4687_BR	DOUBLE[6]	...	For the broad He II λ 4687 component
OIII5007	DOUBLE[6]	...	For the entire [O III] λ 5007 profile
OIII5007C	DOUBLE[6]	...	For the core [O III] λ 5007 profile
CAII3934	DOUBLE[6]	...	For the Ca II K absorption line
OII3728	DOUBLE[6]
NEV3426	DOUBLE[6]	...	For the entire Ne V λ 3426 profile (narrow and broad lines combined)
MGII	DOUBLE[6]	...	For the entire Mg II profile (narrow and broad lines combined)
MGII_BR	DOUBLE[6]	...	For the broad Mg II component
CIII_ALL	DOUBLE[6]	...	For the entire C III] complex (C III], Si III], Al III)
CIII_BR	DOUBLE[6]	...	For the broad C III] component
SIII1892	DOUBLE[6]
ALIII1857	DOUBLE[6]
NIII1750	DOUBLE[6]
CIV	DOUBLE[6]
HEII1640	DOUBLE[6]	...	For the entire He II λ 1640 profile (narrow and broad lines combined)
HEII1640_BR	DOUBLE[6]	...	For the broad He II λ 1640 component
SIIV_OIV	DOUBLE[6]	...	For the 1400 Å complex
OII304	DOUBLE[6]
LYA	DOUBLE[6]
NV1240	DOUBLE[6]
		Å, Å, 10 ⁻¹⁷ erg s ⁻¹ cm ⁻² , [erg s ⁻¹], km s ⁻¹ , Å	Uncertainties in peak wavelength, 50% flux centroid wavelength, flux, logL _{line} , FWHM, rest-frame equivalent width
HALPHA_ERR	DOUBLE[6]
HALPHA_BR_ERR	DOUBLE[6]
NII6585_ERR	DOUBLE[6]
HBETA_ERR	DOUBLE[6]
HBETA_BR_ERR	DOUBLE[6]
HEII4687_ERR	DOUBLE[6]
HEII4687_BR_ERR	DOUBLE[6]
OIII5007_ERR	DOUBLE[6]
OIII5007C_ERR	DOUBLE[6]

Continued on Next Page...

Table 4 – Continued

Column	Format	Units	Description
CAII3934_ERR	DOUBLE[6]
OII3728_ERR	DOUBLE[6]
NEV3426_ERR	DOUBLE[6]
MGII_ERR	DOUBLE[6]
MGII_BR_ERR	DOUBLE[6]
CIII_ALL_ERR	DOUBLE[6]
CIII_BR_ERR	DOUBLE[6]
SIIII1892_ERR	DOUBLE[6]
ALIII1857_ERR	DOUBLE[6]
NIII1750_ERR	DOUBLE[6]
CIV_ERR	DOUBLE[6]
HEII1640_ERR	DOUBLE[6]
HEII1640_BR_ERR	DOUBLE[6]
SIIV_OIV_ERR	DOUBLE[6]
OII304_ERR	DOUBLE[6]
LYA_ERR	DOUBLE[6]
NV1240_ERR	DOUBLE[6]
HA_COMP_STAT	DOUBLE[2]		Complex line pixel number, reduced χ^2
HB_COMP_STAT	DOUBLE[2]		...
CAII3934_LOC_STAT	DOUBLE[2]		Local line pixel number, reduced χ^2
OII3728_LOC_STAT	DOUBLE[2]		...
NEV3426_LOC_STAT	DOUBLE[2]		...
MGII_COMP_STAT	DOUBLE[2]		Complex line pixel number, reduced χ^2
CIII_COMP_STAT	DOUBLE[2]		...
CIV_COMP_STAT	DOUBLE[2]		...
SIIV_COMP_STAT	DOUBLE[2]		...
LYA_COMP_STAT	DOUBLE[2]		...
LOGLBOL	DOUBLE	[erg s ⁻¹]	Bolometric luminosity
LOGLBOL_ERR	DOUBLE	[erg s ⁻¹]	Uncertainties in bolometric luminosity
LOGMBH_HB	DOUBLE	[M _⊙]	Single-epoch BH mass based on H β
LOGMBH_HB_ERR	DOUBLE	...	Uncertainties in LOGMBH_HB
LOGMBH_MGII	DOUBLE	...	Single-epoch BH mass based on Mg II
LOGMBH_MGII_ERR	DOUBLE
LOGMBH_CIV	DOUBLE	...	Single-epoch BH mass based on C IV
LOGMBH_CIV_ERR	DOUBLE
LOGMBH	DOUBLE	...	Fiducial single-epoch BH mass
LOGMBH_ERR	DOUBLE
LOGLEDD_RATIO	DOUBLE		Eddington ratio based on fiducial single-epoch BH mass
LOGLEDD_RATIO_ERR	DOUBLE		Uncertainties in LOGLEDD_RATIO
Z_SYS_LINE	DOUBLE[8]		Systematic redshift from individual lines in the order of H β_{br} , [O III] 5007, Ca II 3934, [O II] 3728, Mg II, C III], C IV, Si IV
Z_SYS_LINE_ERR	DOUBLE[8]		Uncertainties in systematic redshift from individual lines

We compare our spectral measurements with earlier studies on SDSS quasars (e.g., Shen et al. 2011, 2019; Rakshit et al. 2020) and generally find good agreement, despite minor differences in the exact fitting methods. One notable difference is that our global-fitting approach differs from the local-fitting approach in Shen et al. (2011), and the measured C IV FWHMs and fluxes are slightly different from the DR7Q measurements in Shen et al. (2011).

Another major difference is that the DR16Q sample probes much fainter luminosities than the DR7Q sample. While the fiducial BH mass recipes we adopted produce consistent results between two different lines for the luminous subset of DR7Q quasars, the BH mass consistency between two lines is degraded for lower-luminosity objects. In Fig. 9 we compare virial BH masses between two lines covered in the same spectrum. For the DR7Q subset, we reproduce the results in Shen et al. (2011). However, when extending to fainter luminosities of DR16Q quasars, there is a mean offset of $\sim 0.1 - 0.2$ dex between two BH mass estimators. For many low-luminosity DR16Q quasars, we also find that the C IV line has a rather narrow core, potentially arising from the narrow-line region or representing the intrinsic C IV profile. The resulting C IV FWHM is typically narrow and it is unclear if a narrow-line subtraction is necessary when estimating the C IV-based BH masses.

Because the systematic uncertainty for any of the single-epoch virial BH mass recipes is substantially larger (~ 0.4 dex) than typical measurement uncertainties, and because the extrapolation of these mass recipes calibrated with local reverberation mapping AGN samples to distant quasars is highly uncertain (e.g., Shen 2013), in this work we do not attempt to design new single-epoch mass recipes to bring all three estimators (H β , Mg II, and C IV) into agreement for DR16Q quasars. A more reasonable approach is to wait for better single-epoch BH mass recipes suitable for SDSS quasars, which are calibrated using direct reverberation mapping results of luminous quasars (e.g., Shen et al. 2015).

5.2. Spectral diversity of quasars

Broad-line quasars display a range of spectral diversities as well as correlations among physical properties. For example, the strength (equivalent width) of certain broad emission lines is correlated with quasar luminosity (i.e., the Baldwin effect, Baldwin 1977), and many spectral properties correlate with the optical Fe II strength or Eddington ratio of the quasar, known as the Eigenvector 1 correlations (e.g., Boroson & Green 1992; Sulentic et al. 2000; Marziani et al. 2001; Boroson 2002; Richards

et al. 2011; Shen & Ho 2014). The spectral measurements presented here for the DR16Q quasars can be used to perform detailed statistical studies of emission properties of quasars and correlations among them. We present a few examples below.

Fig. 10 displays the distribution of quasars in the optical Fe II strength, defined by $R_{\text{FeII}} \equiv \text{EW}_{\text{FeII}4434-4684} / \text{EW}_{\text{H}\beta, \text{br}}$, versus broad H β FWHM plane. Such a plot was first seen in Boroson & Green (1992) and subsequently utilized in studies of the Eigenvector 1 relations of quasars (e.g., the 4DE1 relations, Sulentic et al. 2000). A general trend of decreasing broad H β width with increasing optical Fe II strength is seen, likely driven by increasing Eddington ratio as R_{FeII} increases (e.g., Boroson 2002; Shen & Ho 2014; Sun & Shen 2015). Orientation of the Balmer broad-line region may also play a role in the vertical dispersion of the distribution (e.g., Wills & Browne 1986; Marziani et al. 2001; Shen & Ho 2014).

In Fig. 11 we show the distribution of quasars in the C IV blueshift versus equivalent width plane, where quasars occupy a similar wedge-shaped region (e.g., Richards et al. 2011; Rivera et al. 2022). The observed overall trend of decreasing C IV EW with increasing C IV blueshift is argued to be driven by accretion parameters (e.g., Richards et al. 2011; Rivera et al. 2022), which also correlates with multi-wavelength quasar properties, in particular X-ray properties (e.g., Rivera et al. 2022).

6. CONCLUSIONS

In this work we compile spectral measurements for 750,414 quasars included in the quasar catalog from SDSS DR16 (Lyke et al. 2020), using optical SDSS spectroscopy. Our final catalog includes continuum and line properties for a list of prominent lines in quasar spectrum, as well as derived quantities such as the black hole mass estimates based on single-epoch mass recipes and Eddington ratios.

This is a major update to the catalog for 105,783 SDSS-DR7 quasars presented in Shen et al. (2011), with a more comprehensive line list and extension to lower quasar luminosities than the DR7 catalog. In particular, we present refined systemic redshifts and more realistic redshift uncertainties for these DR16Q quasars, demonstrating significant improvement over the original redshifts in DR16Q that were largely based on pipeline redshifts.

All products from this work, including the catalog, input fitting parameter files, individual fits output, a python notebook demo, and update notes, can be accessed from https://github.com/QiaoyaWu/sdss4_dr16q_tutorial.

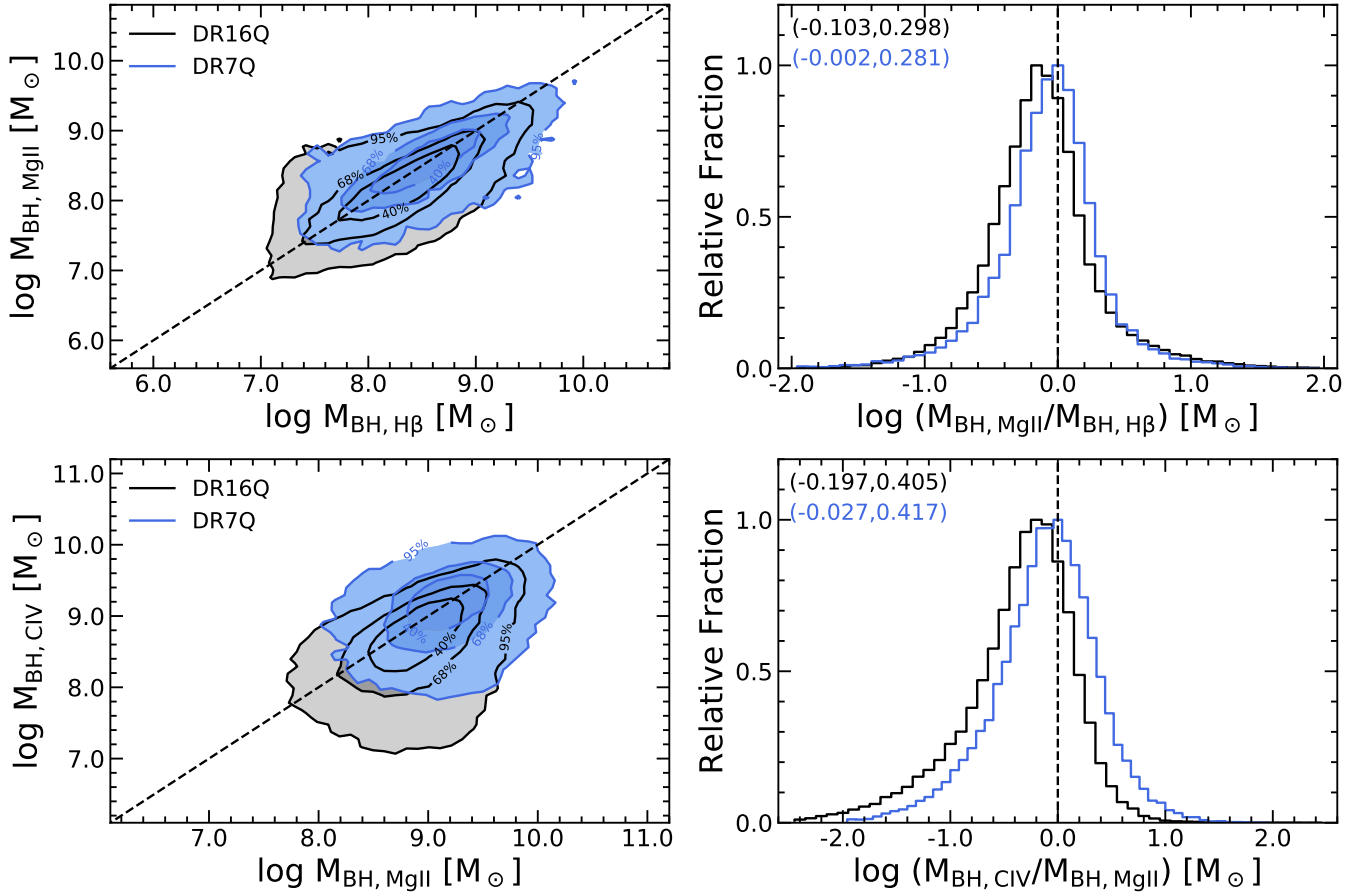


Figure 9. Upper panels: comparison between single-epoch virial black hole masses estimated using the broad Mg II line and broad H β line. The mean (μ) and dispersion (σ) of the mass difference distribution are noted on the top left of the right panel. Lower panels: comparison between virial BH masses estimated from C IV and Mg II. The contour levels correspond to the enclosed percentiles of the sample. While the BH masses are consistent between two line estimators for DR7 quasars (Shen et al. 2011), there are minor offsets in the mean BH mass between two estimators when extrapolating the same mass recipes to lower-luminosity DR16Q quasars.

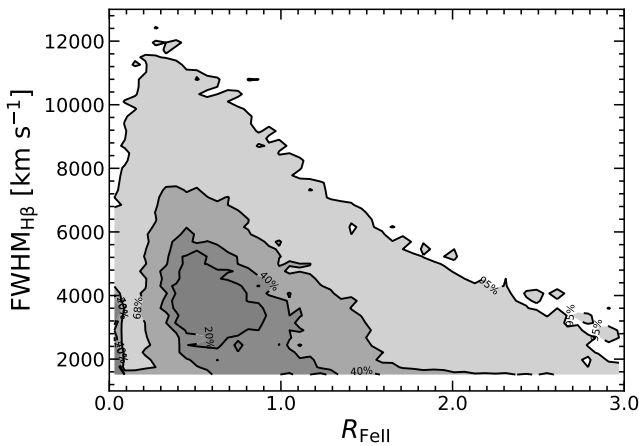


Figure 10. Distribution of DR16Q quasars in the plane of optical Fe II strength (denoted by $R_{\text{FeII}} \equiv \text{EW}_{\text{FeII } 4434-4684} / \text{EW}_{\text{H}\beta, \text{br}}$) versus broad H β FWHM.

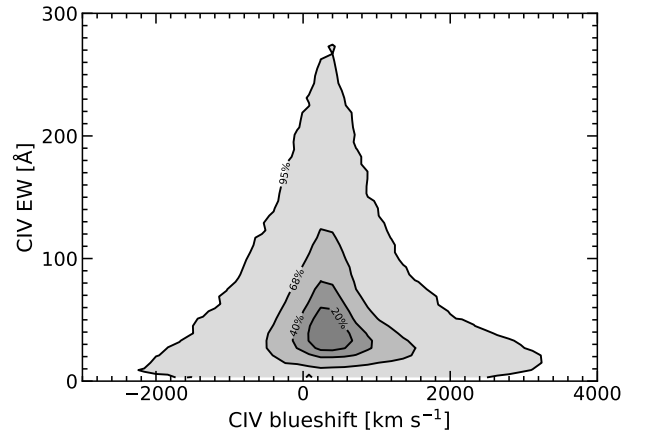


Figure 11. Distribution of DR16Q quasars in the C IV equivalent width versus C IV blueshift (wrt systemic) plane.

This work is partially supported by NSF grant AST-2009947. QW acknowledges support from an Illinois Graduate Survey Science Fellowship.

Funding for the Sloan Digital Sky Survey IV has been provided by the Alfred P. Sloan Foundation, the U.S.

Department of Energy Office of Science, and the Participating Institutions. SDSS-IV acknowledges support and resources from the Center for High-Performance Computing at the University of Utah. The SDSS web site is www.sdss.org.

REFERENCES

- Baldwin, J. A. 1977, *ApJ*, 214, 679
- Blanton, M. R., Bershad, M. A., Abolfathi, B., et al. 2017, *AJ*, 154, 28
- Bolton, A. S., Schlegel, D. J., Aubourg, É., et al. 2012, *AJ*, 144, 144
- Boroson, T. A. 2002, *ApJ*, 565, 78
- Boroson, T. A., & Green, R. F. 1992, *ApJS*, 80, 109
- Cardelli, J. A., Clayton, G. C., & Mathis, J. S. 1989, *ApJ*, 345, 245
- Dawson, K. S., Schlegel, D. J., Ahn, C. P., et al. 2013, *AJ*, 145, 10
- Eisenstein, D. J., Weinberg, D. H., Agol, E., et al. 2011, *AJ*, 142, 72
- Gaskell, C. M. 1982, *ApJ*, 263, 79
- Guo, H., Shen, Y., & Wang, S. 2018, PyQSOFit: Python code to fit the spectrum of quasars, Astrophysics Source Code Library, record ascl:1809.008, , , ascl:1809.008
- Hewett, P. C., & Wild, V. 2010, *MNRAS*, 405, 2302
- Lyke, B. W., Higley, A. N., McLane, J. N., et al. 2020, *ApJS*, 250, 8
- Marziani, P., Sulentic, J. W., Zwitter, T., Dultzin-Hacyan, D., & Calvani, M. 2001, *ApJ*, 558, 553
- Pâris, I., Petitjean, P., Ross, N. P., et al. 2017, *A&A*, 597, A79
- Rakshit, S., Stalin, C. S., & Kotilainen, J. 2020, *ApJS*, 249, 17
- Richards, G. T., Fan, X., Newberg, H. J., et al. 2002, *AJ*, 123, 2945
- Richards, G. T., Lacy, M., Storrie-Lombardi, L. J., et al. 2006, *ApJS*, 166, 470
- Richards, G. T., Kruczek, N. E., Gallagher, S. C., et al. 2011, *AJ*, 141, 167
- Rivera, A. B., Richards, G. T., Gallagher, S. C., et al. 2022, *ApJ*, 931, 154
- Salviander, S., Shields, G. A., Gebhardt, K., & Bonning, E. W. 2007, *ApJ*, 662, 131
- Schlafly, E. F., & Finkbeiner, D. P. 2011, *ApJ*, 737, 103
- Schlegel, D. J., Finkbeiner, D. P., & Davis, M. 1998, *ApJ*, 500, 525
- Schneider, D. P., Richards, G. T., Hall, P. B., et al. 2010, *AJ*, 139, 2360
- Shen, Y. 2013, *Bulletin of the Astronomical Society of India*, 41, 61
- Shen, Y., & Ho, L. C. 2014, *Nature*, 513, 210
- Shen, Y., Richards, G. T., Strauss, M. A., et al. 2011, *ApJS*, 194, 45
- Shen, Y., Brandt, W. N., Dawson, K. S., et al. 2015, *ApJS*, 216, 4
- Shen, Y., Brandt, W. N., Richards, G. T., et al. 2016, *ApJ*, 831, 7
- Shen, Y., Hall, P. B., Horne, K., et al. 2019, *ApJS*, 241, 34
- Smee, S. A., Gunn, J. E., Uomoto, A., et al. 2013, *AJ*, 146, 32
- Sulentic, J. W., Zwitter, T., Marziani, P., & Dultzin-Hacyan, D. 2000, *ApJL*, 536, L5
- Sun, J., & Shen, Y. 2015, *ApJL*, 804, L15
- Tsuzuki, Y., Kawara, K., Yoshii, Y., et al. 2006, *ApJ*, 650, 57
- Tytler, D., & Fan, X.-M. 1992, *ApJS*, 79, 1
- Vestergaard, M., & Peterson, B. M. 2006, *ApJ*, 641, 689
- Vestergaard, M., & Wilkes, B. J. 2001, *ApJS*, 134, 1
- Wills, B. J., & Browne, I. W. A. 1986, *ApJ*, 302, 56